Targeting Glioma Stem Cells through Combined BMI1 and EZH2 Inhibition

Xun Jin[1,2,3], **Leo J. Y. Kim**[1,4,5,6], **Qiulian Wu**[1,6], **Lisa C. Wallace**[1], **Briana C. Prager**[1,4,5,6,7], **Tanwarat Sanvoranart**[1], **Ryan C. Gimple**[1,4,5,6], **Xiuxing Wang**[1,6], **Stephen C. Mack**[1,8], **Tyler E. Miller**[1,4,5], **Ping Huang**[1], **Claudia L. Valentim**[1], **Qi-gang Zhou**[1], **Jill S. Barnholtz-Sloan**[9], **Shideng Bao**[1,7,9], **Andrew E. Sloan**[9,10], and **Jeremy N. Rich**[1,6,7,9]

[1]Department of Stem Cell Biology and Regenerative Medicine, Lerner Research Institute, Cleveland Clinic, Cleveland, OH, USA

[2]Tianjin Medical University Cancer Institute and Hospital, Tianjin, P.R. China

[3]First Affiliated Hospital of Wenzhou Medical University, Wenzhou, Zhejiang, P.R. China

[4]Department of Pathology, Case Western Reserve University, Cleveland, OH, USA

[5]Medical Scientist Training Program, School of Medicine, Case Western Reserve University, Cleveland, OH, USA

[6]Division of Regenerative Medicine, Department of Medicine, University of San Diego, San Diego, CA, USA

[7]Cleveland Clinic Lerner College of Medicine of Case Western Reserve University, Cleveland, OH, USA

[8]Department of Pediatrics, Division of Pediatric Hematology and Oncology, Baylor College of Medicine, Houston, TX, USA

[9]Case Comprehensive Cancer Center, Case Western Reserve University School of Medicine, Cleveland, OH, USA

[10]Department of Neurological Surgery, University Hospitals-Cleveland Medical Center, Cleveland, OH, USA

Abstract

Glioblastomas are lethal cancers defined by angiogenesis and pseudopalisading necrosis. Here, we demonstrate that these histological features are associated with distinct transcriptional programs, with vascular regions showing a proneural profile and hypoxic regions a mesenchymal pattern. As these regions harbor glioma stem cells (GSCs), we investigated the epigenetic regulation of these two niches. Proneural, perivascular GSCs activated EZH2, whereas mesenchymal GSCs in hypoxic regions expressed BMI1 protein, which promoted cellular survival under stress, due to downregulation of the E3 ligase, RNF144A. Using both genetic and pharmacologic inhibition, we found that proneural GSCs are preferentially sensitive to EZH2 disruption, whereas mesenchymal GSCs are preferentially sensitive to BMI1 inhibition. Given that glioblastomas contain both proneural and mesenchymal GSCs, combined EZH2 and BMI1 targeting proved more effective than either agent alone both in culture and in vivo, suggesting that strategies that simultaneously target multiple epigenetic regulators within glioblastomas may be necessary to overcome resistance to therapies caused by intratumoral heterogeneity.

Keywords

Glioblastoma is the most prevalent and lethal primary brain tumor, with current therapies offering only palliation[1]. Glioblastomas represent one of the most rigorously characterized solid cancers, yet delineation of molecular lesions has not translated into effective targeted therapeutics. Glioblastomas display remarkable heterogeneity, both between tumors (intertumoral heterogeneity) and within tumors (intratumoral and cellular heterogeneity), supporting molecular and cellular complexity unlikely to respond to targeting single molecular pathways. Glioblastomas contain stem cell-like tumor initiating cells, GSCs (also known as cancer stem cells)[2,3]. Whereas GSCs remain controversial due to unresolved issues in their definition and origin, the significance of GSCs has been supported by observations that they promote resistance to conventional therapies, invasion into normal brain, and angiogenesis[4–6]. GSCs are not uniformly distributed within tumors, but rather enriched in perivascular and hypoxic niches, suggesting that GSCs critically interact with their microenvironment[6–8]. Indeed, microenvironmental stressors, such as hypoxia, acid, and nutrient restriction, promote GSC maintenance[7,9,10].

Global transcript profiling and DNA methylation analyses from bulk adult glioblastoma samples have categorized glioblastoma into several distinct subtypes: glioma CpG island methylator phenotype (G-CIMP), associated with mutations in isocitrate dehydrogenase 1 or 2 (*IDH1/2*); non-G-CIMP proneural; classical or proliferative; and mesenchymal[11]. Genomic profiling has yet failed to guide precision medicine efforts for glioblastoma[12], possibly because the tumors comprise cell populations with divergent subtype-specific gene expression[13,14]. Glioblastoma transcriptional groups are plastic, including proneural-to-mesenchymal transition after cytotoxic therapy[15,16]. Nevertheless, tumor cells grown under stem cell conditions recapitulate the dominant subtype of parental tumor from which they were derived, suggesting retention of a cell intrinsic biology[17,18]. We hypothesized that the heterogeneous distribution of GSCs suggest that they reside in different niches, requiring differential therapeutic targeting of different subsets in the context of their specific niches.

RESULTS

As bulk tumors contain cells from different subgroups[13], we profiled expression patterns within specific tumor microenvironments by image-guided multiregional glioblastoma sampling (Fig. 1a). Tumor cells from the enhancing region (ER) expressed high levels of proneural genes, whereas the necrotic region (hypoxic; NR) expressed high levels of mesenchymal genes (Fig. 1b). An intermediate tumor region (enhanced margin, EM) displayed a mixed transcriptional signature comprising classical and proneural gene expression signatures (Fig. 1b). These findings were validated in two other multi-regional patient biopsies with glioblastoma subtype gene signatures (Supplementary Fig. 1). GSCs displayed regional variation, measured by immunofluorescence of each region using proneural GSC markers, SOX2 and OLIG2, and mesenchymal GSC markers, CD44 and YKL40[16,19]. GSCs in the ER, defined by disruption of the blood-brain barrier at areas of angiogenesis, were exclusively SOX2$^+$ and OLIG2$^+$, whereas NR GSCs exclusively CD44$^+$ and YKL40$^+$, indicating segregation of proneural and mesenchymal GSC markers (Fig. 1c). Gene expression profiling for vascular and hypoxic markers confirmed that proneural-enriched cells were associated with vascular regions, and mesenchymal cells with hypoxia (Fig. 1d). Immunofluorescence staining using von Willebrand Factor (vWF) for vessels and carbonic anhydrase 9 (CA9) for hypoxia confirmed the regional variance of vascularity and hypoxia (Fig. 1e). To validate our observations in a larger tumor cohort, we interrogated the Ivy Glioblastoma Atlas Project (Ivy GAP) database, which contains data from 55 glioblastomas regionally microdissected with RNA sequencing (RNA-seq) (http://glioblastoma.alleninstitute.org/). Confirming our findings from the MRI-guided biopsy results, the leading edge and infiltrating tumor regions expressed a proneural signature, whereas perinecrotic and microvascular proliferative regions expressed a mesenchymal signature (Fig. 1f–h).

Next, we constructed microenvironment-related gene signatures based on microarray data from vascular sources [human umbilical vein endothelial cells (HUVEC) and human microvascular endothelial cells (HMVEC)] and glioblastoma hypoxia vs. normoxia analyses[20,21] (Supplementary Fig. 2a, 2b, 3a and 3b). Selected signatures and genes were analyzed in glioblastoma samples and the Ivy GAP database (Supplementary Fig. 2c, 2f, 2i, 3c and 3f). In The Cancer Genome Atlas (TCGA) low-grade glioma-glioblastoma database, both vascular signatures and hypoxia were expressed in glioblastoma (Supplementary Fig. 2d, 2g and 3d), and associated with tumor histology, grade, and defining molecular features (Supplementary Fig. 4a). Proneural glioblastomas expressed markers of mature vessels, whereas mesenchymal glioblastomas expressed markers for microvasculature and hypoxia[22,23] (Supplementary Fig. 2e, 2h, and 3e). Both vascular signatures and hypoxia were each significantly anti-correlated with patient survival (Supplementary Fig. 2j, 2k and 3g). Patients with both vascularity and hypoxia expression patterns fared the worst (Supplementary Fig. 4b), supporting microvascular and hypoxic microenvironments as major predictors of unfavorable glioblastoma patient survival[24,25]. Our multi-regional patient biopsy samples validated these in silico observations, demonstrating that the regional variation in transcriptional signatures correlated with vascular and hypoxic features (Supplementary Fig. 4c and 4d).

Regional transcriptional variation may reflect differential chromatin regulation. Polycomb repressive complexes (PRCs) comprise major chromatin modifiers of epigenetic regulation of global gene expression. PRC1 and PRC2 collectively regulate chromatin compaction through specific histone modifications: PRC2 first binds to chromatin and its catalytic subunit, EZH2, trimethylates H3K27. H3K27me3 is then recognized by PRC1, which contains BMI1, followed by monoubiquitination of histone 2A on lysine 119 (H2AK119Ub) to cause chromatin compaction and pausing of RNA polymerase II. However, recent evidence suggests that PRC1 can also silence gene expression through a non-canonical, H3K27me3-independent mechanism[26]. Based on this background, we investigated PRC1 and PRC2 activity with H2AK119Ub and H3K27me3 staining in multiregional patient biopsy samples, observing dichotomous distribution of H2AK119Ub and H3K27me3 positive cells in hypoxic (necrotic) and vascular (enhancing) regions, respectively (Fig. 2a and Supplementary Fig. 5a). As the GSC markers CD133 and CD44 may be specific for glioblastoma subgroup[16], we employed another GSC marker, CD15 (stage-specific embryonic antigen-1 (SSEA1))[34], which we find is less specific, but more sensitive than CD133 (data not shown). CD15$^+$ cells in different regions expressed H2AK119Ub or H3K27me3 and displayed functional characteristics of GSCs (Fig. 2a and Supplementary Fig. 5a–c). Using image-guided biopsies from two new glioblastomas, we interrogated genome-wide distribution of chromatin marks from PRC1 (H2AK119Ub[28]) or PRC2 (H3K27me3) in CD15$^+$ GSCs from enhancing and necrotic regions using chromatin immunoprecipitation followed by deep sequencing (ChIP-seq). To determine region specific peaks, we analyzed overlapping peaks in both patient specimens and identified peaks that were both unique to a particular anatomic region and shared between patient specimens (Fig. 2b). Annotation of region-specific target genes of H3K27me3 or H2AK119Ub with overlapping peaks in a same anatomic region revealed over 80% of region-specific target genes displayed differential H3K27me3 or H2AK119Ub marks (Fig. 2c and Supplementary Table 1), indicating distinct PRC function in GSCs residing in different regions. While intertumoral variation was substantial, shared regions converged on important gene targets. H3K27me3, generally associated with inhibition of transcription, marked neuronal and cellular development targets in both the ER and NR, albeit without substantial overlap in gene identity, with EZH2/SUZ12/H3K27me3 targets most significantly in the ER (Fig. 2d and Supplementary Table 1). In contrast, H2AK119Ub marked very different targets in the ER and NR, with H2AK119Ub in CD15$^+$ GSCs from the hypoxia (necrotic) regions marking genes strongly associated with mesenchymal signaling pathways, such as TGFβ, NFκB, and WNT (Fig. 2d and Supplementary Table 1), indicating probable microenvironment-specific functions of PRC2 and PRC1. Furthermore, an EZH2 activation signature (containing 41 putative targets or partners of EZH2[36]) and EZH2 protein levels were significantly enriched in tumors with proneural signatures or high expression of OLIG2, a proneural marker (Fig. 2e, 3a and Supplementary Fig. 6g), whereas a BMI1 activation signature (containing 341 genes downregulated upon BMI1 knockdown[37]) and BMI1 protein levels were significantly enriched in tumors with mesenchymal transcriptional profiles or high expression of CD44, a mesenchymal marker (Fig. 2f, 3a, and Supplementary Fig. 7g).

To assess PRC contribution to microenvironment-specific distribution of glioblastoma subtypes, we correlated EZH2, BMI1, and microenvironment-related signatures. The EZH2 activation signature positively correlated with proneural and mature vascular signature, but negatively correlated with mesenchymal and classical microenvironment signatures (Supplementary Fig. 6f, 8b, and 8c), implicating EZH2 function in tumor neovascular regions[31]. Conversely, a BMI1 activation signature correlated positively with mesenchymal or classical microenvironment signatures and negatively with a proneural microenvironment signature (Supplementary Fig. 7f, 8b, and 8c). EZH2 and BMI1 protein or activation signatures were each associated with poor prognosis, but the worst prognosis was associated with high expression levels of both proteins or signatures (Fig. 3b, Supplementary Fig. 6e, 6h, 6i, 7e, 7h, 8a, and 8d), suggesting that combined PRC1–PRC2 activation portends greater tumor malignancy.

As both EZH2 and BMI1 regulate GSCs, we investigated BMI1 and EZH2 levels in several validated proneural and mesenchymal GSC and neural progenitor cell models. BMI1 and H2AK119Ub were markedly increased in CD44^{+} and YKL40^{+} mesenchymal GSCs, whereas EZH2 and H3K27me3 were associated with OLIG2^{+} and SOX2^{+} proneural GSCs (Fig. 3c). RNA-seq data from 19 patient-derived GSC models that we generated confirmed *EZH2* mRNA and activity signatures correlated with a proneural signature, while BMI1 activation, but not *BMI1* mRNA, correlated with mesenchymal GSCs (Supplementary Fig. 9), indicating that BMI1 and EZH2 signaling pathways were activated in different GSC subtypes.

EZH2 mRNA expression levels correlated with the EZH2 activation signature and the proneural subtype and microenvironment in TCGA tumor samples (Supplementary Fig. 6), but, surprisingly, *BMI1* mRNA expression did not correlate with a BMI1 activation signature or the mesenchymal subtype/microenvironment signature (Supplementary Fig. 7), suggesting that EZH2 is regulated at the transcriptional level but BMI1 is regulated post-transcriptionally. Inhibiting translation with cycloheximide treatment showed that BMI1 protein levels were unchanged in mesenchymal GSCs, but markedly reduced in proneural GSCs (Supplementary Fig. 10a). Conversely, poly-ubiquitinated BMI1 was strongly increased in proneural GSCs after treatment with the proteasome inhibitor lactacystin, but weakly accumulated in mesenchymal GSCs under the same conditions (Fig. 3d), suggesting that ubiquitin-mediated proteolysis maintains BMI1 protein stability in GSCs of different subtypes.

Based on apparent region-specific BMI1 proteosomal degradation, we interrogated the TCGA glioblastoma database for ubiquitin-related genes whose expression correlated inversely with BMI1 activation. Among 254 genes associated with ubiquitination, 22 genes were differentially expressed by proneural and mesenchymal glioblastomas (Supplementary Fig. 10b). To link these genes to BMI1 activity, we plotted r values for the 22 genes against two BMI1-related signatures (Fig. 3e). The top r value negatively associated with BMI1 activation was associated with the ring finger, RNF144A, which was previously described as a E3 ligase for the DNA-dependent protein kinase, catalytic subunit DNA-PKcs[39]. Supporting its potential role as a BMI1 E3 ligase, RNF144A expression negatively correlated with BMI1 activation and positively correlated with a BMI1 inhibition signature

(Fig. 3e). ChIP-seq for acetylation of histone H3 lysine 27 (H3K27ac) on a panel of glioma GSCs and primary patient glioblastoma tissues with proneural or mesenchymal signatures were then compared to deposited results for other gliomas and normal brain. CD44 showed preferential activation in mesenchymal models, whereas OLIG2 was more specific for proneural tumors (Supplementary Fig. 10c). RNF144A transcriptional regulation was stronger in proneural models and correlated with SOX2 (Supplementary Fig. 10c). Supporting a negative regulatory role of RNF144A on BMI1 protein levels, mesenchymal GSCs expressed lower RNF144A protein levels compared to normal neural precursors and proneural GSCs (Supplementary Fig. 10d). Immunoprecipitation confirmed direct binding of RNF144A to BMI1 (Supplementary Fig. 10e). Depleting RNF144A in proneural GSCs with low baseline levels of BMI1 reduced poly-ubiquitinated BMI1 after proteolysis inhibition and concordantly increased non-ubiquitinated BMI1 protein expression (Fig. 3f). Non-ubiquitinated BMI1 protein in RNF144A knockdown cells persisted at similar levels with or without proteolysis inhibition (Supplementary Fig. 10f), highlighting RNF144A-mediated poly-ubiquitination as a regulatory node for BMI1 protein degradation.

To determine the clinical relevance of RNF144A in gliomas, we examined its regulation and survival in patient tissues and databases. RNF144A expression was lower in glioblastoma than low grade gliomas (LGG) and inversely related to patient survival (Supplementary Fig. 11a–d). Using the LGG-glioblastoma TCGA dataset, we mapped the mRNA expression levels for *RNF144A* and *EZH2* against tumor histology, grade, survival, and common molecular features (*IDH1* or *ATRX* mutations; chromosome 1p and 19 co-deletion) (Supplementary Fig. 12a). RNF144A mRNA levels were strongly inversely correlated with glioblastoma histology and IDH1 mutation, with a weaker association with chromosome 1p and 19q co-deletion. *RNF144A*^{low}*EZH2*^{high} tumors were enriched with unfavorable microenvironmental transcriptional signatures (Supplementary Fig. 12b). To determine the prognostic significance of *RNF144A* and *EZH2* mRNA levels, we mapped expression levels for each targets and derived survival trends, revealing that *RNF144A*^{low}*EZH2*^{high} tumors had the lowest survival (Supplementary Fig. 12c). Multivariate analysis considering patient age, tumor grade, and *IDH* mutation revealed *RNF144A* mRNA and BMI1 activation signatures as independent prognostic factors for overall survival of glioma prognosis (Supplementary Table 2), but not for glioblastoma (Supplementary Table 3). Collectively, suppression of RNF144A informs tumor grade and poor patient outcome, supporting a negative role in tumor malignancy.

To determine a functional role for differential PRC utilization by GSCs, we examined EZH2 and BMI1 expression in GSCs and neural precursors under stressful conditions, including hypoxia and nutrient restriction: neural precursors and proneural GSCs lost BMI1 and EZH2 expression, with loss of proneural GSC markers (Fig. 3g). In contrast, mesenchymal GSCs under stress retained BMI1 expression and increased levels of mesenchymal markers (Fig. 3g). Mesenchymal GSCs preferentially survived stress, whereas almost all neural precursors and proneural GSCs died (Fig. 3h). Thus, stress conditions, similar to those found in the pseudopallisading necrotic regions, may select for BMI1^{high} mesenchymal glioma cells. Under low stress, RNF144A depletion in proneural GSCs increased BMI1 expression but did not alter cell proliferation or self-renewal, suggesting that BMI1 is not essential in the absence of stress (Supplementary Fig. 13a and 13b). In contrast, targeting RNF144A

expression in proneural GSCs under stress increased cell survival (Supplementary Fig. 13c). To further assess PRC function under stress, we depleted either EZH2 or BMI1 using two non-overlapping specific shRNAs for each target in two proneural (Supplementary Fig. 14a) and two mesenchymal GSC models (Supplementary Fig. 14b). Targeting BMI1 or EZH2 protein levels and chromatin effects was confirmed on immunoblot, measured by their respective modifications, H2K119Ub and H3K27me3. BMI1 depletion potently decreased cell viability of mesenchymal GSCs under stress, with modest or no effects on proneural GSCs (Supplementary Fig. 14c). In contrast, EZH2 depletion failed to sensitize GSCs to harsh growth conditions, suggesting that EZH2 is dispensable under stress. To further support these findings, forced BMI1 expression in proneural GSCs significantly increased cell viability under stress, without altering cell growth or tumorsphere formation in the absence of stress (Supplementary Fig. 14d–g).

To determine the potential role of BMI1 in mediating in vivo tumor growth mimicking regional tumor growth, we performed an in vivo cell mixing experiment with orthotopic co-implantation of BMI1-overexpressing mCherry[+] proneural GSCs and control GFP[+] proneural GSCs (Supplementary Fig. 14h). BMI1^{+} cells significantly accelerated disease progression compared to GFP[+] control proneural GSCs (Supplementary Fig. 14i). BMI1-overexpressing cells preferentially localized to CA9^{+} hypoxic regions in the subsequent brain tumors (Supplementary Fig. 14j), suggesting that BMI1 confers tumor cell fitness in the hypoxic niche. In line with the preferential expression of EZH2 in proneural cells, RNA interference using two non-overlapping shRNAs against EZH2 preferentially reduced cell growth and tumorsphere generation of proneural GSCs (Fig. 4a and 4b). Reciprocally, BMI1 depletion preferentially reduced mesenchymal GSC cell growth and tumorsphere formation (Fig. 4a and 4b), demonstrating differential sensitivity to PRC depletion based on molecular subtypes. Collectively, these results support a context-specific role for BMI1, suggesting that differential utilization of PRCs may contribute to divergent subtype-specific niche adaptation and associated poor prognosis.

To leverage our findings for clinical application, we examined the sensitivity of GSC subtypes to inhibitors of BMI1 (PTC596, denoted as BMI1-i) or EZH2 (EPZ6438, denoted as EZH2-i). Mesenchymal GSCs displayed preferential sensitivity to BMI1-i treatment with an IC_{50} of BMI1-i fourfold lower than the IC_{50} of proneural GSCs and a neural precursor line (Fig. 4c and 4d). Conversely, proneural GSCs were generally more sensitive to EZH2 inhibitor treatment. Differential sensitivity to BMI1 and EZH2 inhibitors was confirmed using the mean IC_{50} of BMI1 (122 nM) and EZH2 (45 μM) inhibitors in proneural and mesenchymal GSCs, respectively (Supplementary Fig. 15a). To determine combinatorial efficacy, we interrogated the effects of a range of concentrations of each inhibitor against two proneural and two mesenchymal GSC models (Supplementary Fig. 15b and 15c). While the interaction did not achieve synergy, the combination of low, clinically achievable concentrations of BMI1 and EZH2 inhibitors completely blocked tumorsphere formation and eradicated the GSC population (Fig. 4e). As all drugs may have off-target effects, we validated the subtype specific effect of BMI1 and EZH2 inhibitors on cell viability and tumorsphere-forming ability with other structurally unrelated inhibitors: PTC209 (another BMI1 inhibitor) and DZNep (another EZH2 inhibitor) (Supplementary Fig. 16).

Systemically delivered drugs against brain tumors must achieve intracranial delivery, as even contrast enhancing gliomas, representing a disrupted blood-tumor barrier, usually have regions of tumor protected by a barrier. To augment the brain penetration of the EZH2i, we leveraged a previously developed approach using a combination with Elacridar (a dual ABCCB1 and ABCG2 inhibitor)[40]. Measurement of the plasma and brain levels of BMI1i after treatment BMI1 and EZH2 inhibitors demonstrated that at least 20% BMI1i blood levels penetrate into the brain (Supplementary Fig. 17a and 17b). To determine if the concentrations achievable in the brain were efficacious, we plotted the measured concentrations of BMI1 and EZH2 inhibitors in the brain against the combinational efficacy studies on four different subtype GSCs, consistent with an 80% *in vitro* inhibitory concentration (Supplementary Fig. 16d, 17a, and 17b)[40]. Pharmacodynamics analysis of each agent against intracranial models over a time course confirmed that BMI1 and EZH2 inhibitors specifically attenuated H2K119Ub and H3K27me3 in tumor tissues obtained from orthotopic tumors (Supplementary Fig. 17c–e).

Leveraging evidence that the BMI1 and EZH2 inhibitors penetrate into the brain, we examined the therapeutic effects of BMI1 and EZH2 inhibitors on mice bearing intracranial tumors derived from proneural, mesenchymal, or mixtures of proneural and mesenchymal GSCs (Fig. 5a and Supplementary Fig. 18a). Though near the limit of detection, bioluminescent imaging confirmed that anti-tumor effects of EZH2 inhibition were more effective against proneural models than mesenchymal models, whereas BMI1 inhibition displayed the opposite predilection, with combined therapy being more effective (Fig. 5b, Supplementary Fig. 18b–e, and Supplementary Fig. 19). To address the *in vivo* cellular effects of the EZH2 or BMI1 inhibitor treatments, we xenografted a combination of mCherry[+] proneural and GFP[+] mesenchymal GSCs, treated with vehicle control or the inhibitors as monotherapy or in combination and analyzed the treated tumors (Supplementary Fig. 20). In mCherry^{+} proneural cells, EZH2i treatment specifically reduced the number of cells with the PRC2 mark H3K27me3, the GSC marker CD15, and the cell proliferation marker Ki67; whereas, there were much more modest changes in mesenchymal cells. In contrast, BMI1i treatment ablated the mesenchymal population. The combination of the BMI1 and EZH2 inhibitors had effects on each marker in both compartments. Cell apoptosis, as measured by active CASPASE3, and senescence, as measured by senescence associated β-GAL, did not show substantial changes with any of the therapies tested. Further, we quantified the residual number of each fluorescently labeled tumor cell population after each therapy, confirming preferential activity of each inhibitor of the specific tumor subtype and superiority of combined treatment (Fig. 5c). These in vivo results translated into superior survival of combined treatment (Fig. 5d–f), indicating that the combinatorial inhibition of BMI1 and EZH2 is an effective treatment strategy for heterogeneous microenvironment-dependent subtype glioblastoma.

DISCUSSION

Tumor cell heterogeneity arises from variation in genetics, epigenetic cell state, and microenvironment. Single cell RNA sequencing of gliomas demonstrated intratumoral variation in transcription profiles with a fraction of proliferating cells that express stem cell programs[13]. Multiple GSC clones can be derived from a single patient[14,35,36]. Our results

refine these observations by linking spatially defined, radiographic features to GSCs with specific transcriptional signatures and response to targeted therapies. We recently reported that mesenchymal GSCs have hypomethylated DNA, associated with reduced availability of methionine and hypoxic induction of methyltransferases that deplete methyl donors[37], suggesting that regional epigenetic regulation could extend to DNA methylation. Here, we find that stress responses may select for different dependencies on PRCs, with PRC1 (BMI1) promoting cellular survival in areas of low oxygen and nutrient availability. Collectively, these findings support a model in which hypoxia promotes the survival of mesenchymal GSCs by repressing the expression of RNF144A that results in enhanced BMI1 protein stability. Like neural stem cells, GSCs receive maintenance cues from their microenvironment; yet GSCs are not passive recipients of these cues, but rather actively remodel their environment through induction of angiogenesis and other features[38]. As we and others have found that hypoxia, acidic stress, and nutrient restriction promote GSC maintenance, the RNF144A-BMI1 regulatory mechanism may empower GSCs to reside in stressful microenvironments.

The significance of epigenetic diversity in tumors is supported by genetic observations that collectively 40% of glioblastomas harbor mutations in epigenetic regulators, including BMI1 and EZH2[39]. Epigenetic dysregulation may induce neoplasia and be amenable to therapeutic targeting, but likely do not adhere to a simple dichotomization of mutations into oncogenes and tumor suppressors, rather permitting cellular plasticity to accelerate tumor evolution. *IDH1* mutations transform astrocytes through modulation of DNA methylation[40]. Mutant IDH1 inhibitors attenuate tumor growth of gliomas harboring *IDH1* mutations[41]. Pediatric glioblastomas are commonly driven by mutations in variant histones, which lead to alterations in DNA methylation and transformation[42–44]. Epigenetic regulators may be particularly effective to target as oncogenic pathways converge on the epigenome to maintain neoplasia[45]. BMI1 regulates tumor initiation and growth in a genetically engineered murine model of glioblastoma and human stem-like glioma lines[46–49]. BMI1 binds and regulates the promoters of numerous genes, including transforming growth factor-β (*TGFβ*), which has been strongly linked to a mesenchymal phenotype[50]. Targeted therapies against BMI1 have shown preclinical efficacy in a number of cancer types, with effects against cancer stem cells[51]. EZH2 has also been investigated as a cancer therapeutic target with numerous studies suggesting potential therapeutic benefit against adult and pediatric high grade gliomas[52–57]. The dynamic interchange of elements between PRC1 and PRC2 suggests that the roles of BMI1 and EZH2 are not biochemically interchangeable, but may permit a plasticity of cell state under different microenvironmental conditions. Our results support a model in which GSCs are present in different niches with differential utilization of BMI1 and EZH2 (Supplementary Fig. 21). Thus, differential region-specific dependency on epigenetic modifiers may inform the development of a combinatorial treatment approach that could collapse intratumoral heterogeneity and limit adaptation to cancer therapeutics.

Comparatively, far less is understood about Ring Finger protein 144A (RNF144A) beyond its enzymatic function. RNF144A is an E3 ligase for DNA-PKcs[39]. Interrogation of the cBioPortal database shows that several cancer types have mutations or amplifications in RNF144A, including prostate, breast, uterine, and lung (data not shown). A single low-grade

glioma patient had a missense mutation and the TCGA glioblastoma data revealed one patient each with a deletion, amplification, and nonsense mutation (data not shown). Prior reports investigating *BMI1* mRNA expression supported increased expression in proneural tumors, but our results demonstrate that BMI1 activity does not correlate with *BMI1* mRNA levels and that BMI1 protein levels are higher in mesenchymal tumors than proneural tumors. RNF144A post-translational regulation of BMI1 provides a novel mechanism of BMI1 regulation in glioblastoma, and reveals a limitation of transcriptional target discovery. Moreover, the clinical relevance of the RNF144A and BMI1 activation signatures inform biomarker development for BMI1 inhibitors.

Our results demonstrate the significant efficacy of combined inhibition of BMI1 and EZH2, but we did not detect cures: the efficacy against each subtype was preferential, but not absolute. Though monotherapy alone against either PRC component hindered tumor growth near the limits of detection, combinatorial therapy against both proneural and mesenchymal tumors achieved the most efficacious tumor control. Glioblastoma cells can undergo molecular subtype transitions under the influence of different tumor microenvironment that may lead to different effects between *in vitro* and *in vivo* experiments by BMI1 and EZH2 inhibitor treatments. Future studies will determine how interconversion of different pools of GSCs may support adaptive resistance to targeted therapies. While our therapeutic paradigm will likely evolve before direct clinical application, our findings suggest that epigenetic therapies against heterogeneous tumors may need to be considered in combination. Both BMI1 and EZH2 contribute to resistance to radiation and chemotherapy, suggesting that our dual targeting strategy may be useful in combination with conventional therapies[55,58,59]. Similar to our prognostic findings, the combined expression of BMI1 and EZH2 in bulk tumor may have greater negative prognostic significance than either target alone[60]. As single tumors may contain different pools of GSCs, we advocate considering not only combined targeting of epigenetic processes, which may prevent the plasticity of cell state transitions, but also GSC pools.

ONLINE METHODS

Human glioblastoma specimens

Excess tumor tissues were collected from glioblastoma patients from whom informed consent was obtained in accordance with approved Institutional Review Board protocols from Cleveland Clinic, Duke University, or University Hospitals-Cleveland Medical Center (UH-CMC). At UH-CMC, the surgeon selected only tumors with significant quantities of enhancing tumor; peritumor regions, which were non-enhancing on T1 weighted MRI with gadolinium but hyperintense on FLAIR imaging and thought to contain infiltrating tumor cells; and necrotic avascular regions in the center of the tumor (enhancing region, enhancing margin, and necrotic region respectively as indicated in Fig. 1). Prior to surgery, the surgeon obtained volumetric imaging of the patient and pre-selected distinct areas of enhancing, necrotic and invading tissue to sample according to his surgical strategy. In the operating room, after co-registration was confirmed to be accurate (BrainLab Stealth), the surgeon then sampled regions from these distinct areas using stereotactic techniques at the beginning

of the procedure. These distinct specimens from different anatomic regions of each tumor were then processed separately and analyzed as indicated below.

Cells and culture condition

Fresh CD15+ GSCs from CW2451, CW2472, and CW2473 glioblastoma primary specimens were isolated with magnetic columns (MACS, CD15 microbeads, Miltenyi Biotec, 130-046-601), and functionally validated self-renewal ability with Limited dilution assay (LDA). Cultures enriched or depleted for GSCs (PN1919, PN3691, PN1914.2, MES3565, MES738, and MES3128) were isolated from surgical specimens or xenografts and functionally validated, as previously described[5–7]. Functional assays included prospective enrichment of stem cell marker expression, sphere formation, and in vivo tumor formation. Cellular contamination was ruled out by serial short tandem repeat (STR) analysis and mycoplasma testing. Molecular subtyping was performed by either expression array or RNA sequencing. The subtype-characterized GSCs (PN11, PN23, PN-JK2, PN-MMK1, MES20, MES28, and MES-MN1) were a generous gift from Erick P. Sulman (M.D. Anderson Cancer Center) or Andrew W. Boyd (Queensland Institute of Medical Research). Normal neural progenitor cells [NPC1 (NHP1), NPC2 (NPC16357), and NPC3 (NPC17893)] and GSCs were maintained in Neurobasal medium with B27 (without vitamin A, Invitrogen), basic fibroblast growth factor (20 ng/ml) and epidermal growth factor (20 ng/ml).

Quantitative RT-PCR

Total RNA was isolated with the RNeasy kit (Qiagen) and reverse-transcribed into cDNA using the aScript cDNA SuperMix (Quanta Biosciences). Real-time PCR was performed on an Applied Biosystems 7900HT cycler using SYBR-green Mastermix (SA Biosciences). Expression values were normalized to *18S*. Gene-specific primers as follows: *18S* forward 5′-TGCATGGCCGTTCTTAGTTG-3′ and reverse 5′- AGTTAGCATGCCAGAGTCTC-3′; *DLL3* forward 5′-CCTGCGCGCTGAATGTC-3′ and reverse 5′-CATCGAAACCTGGAGAGAGG-3′; *OLIG2* forward 5′-CTGGCGTCCGAGTCCAT-3′ and reverse 5′-CCTGAGGCTTTTCGGAGC-3′; *ASCL1* forward 5′-CAACGCCACTGACAAGAAAG-3′ and reverse 5′-GGAGCTTCTCGACTTCACCA-3′; *CD133* forward 5′-TTTTGGATTCATATGCCTTCTGT-3′ and reverse 5′-ACCCATTGGCATTCTCTTTG-3′; *FOXO3* forward 5′-GGTGAATTTCCAATCATCAGC-3′ and reverse 5′-CGAGCTATAGACACCCTGAATG-3′; *MBP* forward 5′-AGGTCTCGTTCCGTGCTG-3′ and reverse 5′-GCCACCATCCCTTGTGAG-3′; *GABRB2* forward 5′-GGAACAATACTACCTAAGGACAA-3′ and reverse 5′-AGTTTGCAACTTAAATCTCAGTT-3′; *PDGFA* forward 5′-GACCGATCCTCAAGCATCTC-3′ and reverse 5′-AAGGACAAGCGGACAAAATG-3′; *NES* forward 5′- GCAGCAGGAAATATGGGAAG-3′ and reverse 5′-TCTCATGGCTCTGGTTTTCC-3′; *EGFR* forward 5′-CTCCGTTTCTTCTTTGCCCAG-3′ and reverse 5′-GCACAAGCCACAAGTGTTCC-3′; *AKT2* forward 5′-ACATCATCTCGTACATGACCAC-3′ and reverse 5′-CTCTGCAAAGAGGGCATCAG-3′; *CD44* forward 5′-TGACACTGTCCAAAGGTTTTC-3′ and reverse 5′-TCACTAATAGGGCCAGCCTC-3′; *YKL40* forward 5′-CCAAGGAGCCAAACATCCTA-3′ and reverse 5′-

GAAGGGGAAGTAGGATAGGGG-3′; *TIMP1* forward 5′-
TGGTAACTCTTTATTTCATTGTCCG-3′ and reverse 5′-
CTGAAAAGGGCTTCCAGTCC-3′; and *TGFβ1* forward 5′-
GCCAGATCCTGTCCAAGCTG-3′ and reverse 5′-GGTGACCTCCTTGGCGTAGTA-3′;
CA9 forward 5′-ACCTGGTGACTCTCGGCTACAG-3′ and reverse 5′-
CAGCCAGGCAGGAATTCAGC-3′; *GLUT3* forward 5′-
AGCTCTCTGGGATCAATGCTGTGT-3′ and reverse 5′-
ATGGTGGCATAGATGGGCTCTTGA-3′; *GLUT1* forward 5′-
TCATCGTGGCTGAACTCTTC-3′ and reverse 5′-GATGAAGACGTAGGGACCAC-3′;
HIF1α forward 5′-CCTATGTAGTTGTGGAAGTTTATGC-3′ and reverse 5′-
ACTAGGCAATTTTGCTAAGAATG-3′; *MCT1* forward 5′-
TGTAATCTACCAGTGGTGCTC-3′ and reverse 5′-AACCTACTTCTTTCCCCCATC-3′;
MCT4 forward 5′-GGGTCATCACTGGCTTGGGT-3′ and reverse 5′-
GGAACACGGGACTGCCTGC-3′; *LDH5* forward 5′-TGCTGTACGTACTGCATTTGC-3′
and reverse 5′-ATCCCAGGATGTGACTCACTG-3′; *CD31* forward 5′-
AAGGCCAGATGCACATCC-3′ and reverse 5′-
TTCTACCCAACATTAACTTAGCAGG-3′; *VEGFR2* forward 5′-
TAGCATGTCTTATAGTCATT-3′ and reverse 5′-CACTCTCTGAATGATTATTA-3′; *CD34*
forward 5′-CCGTCATTGAAACCAGG-3′ and reverse 5′-
TCATAGCCCAGATCAGCTC-3′; *ACTIN* forward 5′-AGAAAATCTGGCACCACACC-3′
and reverse 5′- AGAGGCGTACAGGGATAGCA-3′; *VEGFB* forward 5′-
CCATCTCTTTTATCAGGGTTGG-3′ and reverse 5′-
CTCTGTGCAAGTAAGCATCTTACA-3′.

Western blot analysis and immunoprecipitation assay

Cells were collected and lysed in IP Lysis buffer (Thermo Scientific) containing phosSTOP
phosphatase inhibitor cocktail (Roche) and protease inhibitor cocktail (Sigma, St. Louis) and
separated by 12% sodium dodecyl sulfate polyacrylamide gel electrophoresis (NuPAGE Bis-
Tris gel, Invitrogen) and transferred to PVDF membranes (Millipore). Membranes were
blocked with 5% (wt/vol) non-fat milk in PBS-Tween-20 (0.5% vol/vol) and probed with
primary antibodies against BMI1 (1:1000, Abcam, ab126783), H2K119Ub (1:1000, Cell
signaling, #8240S), CD44 (1:1000, BD Biosciences, 550392), YKL40 (1:1000, Abcam,
ab86428), EZH2 (1:1000, BD Biosciences, 612667), H3K27Me3 (1:1000, Millipore,
07-689), OLIG2 (1:1000, R&D system, AF2418), SOX2 (1:1000, R&D system, AF2018),
RNF144A (1:500, Abcam, ab89260), Ub (1:5000, Santa Cruz, sc-9133), TUBULIN (α-
Tubulin,1:10,000, Sigma-Aldrich, T6074), and ACTIN (β-actin,1:10,000, Sigma-Aldrich,
A1978). BMI1-RNF144A interaction and BMI1 polyubiquitination were detected by Pierce
Crosslink magnetic IP and Co-IP kit (Thermo Scientific). For the ubiquitination assays, cells
were treated with Lactacystin (5 μM or 10 μM; Sigma) for 5hr before collection. BMI1
polyubiquitination was quantified by Image J.

Immunofluorescence and β-GAL staining

10 μm thick slides of de-identified frozen multi-regional samples [glioblastoma patient
(CW1757) according T1-weighted MRI images] and PN3691 (VEC/BMI1) xenografted
frozen brain tissue were fixed in 4% paraformaldehyde and immunolabeled using the

primary antibodies against SOX2 (1:500, R&D system, AF2018), CD44 (1:100, BD Biosciences, 550392), vWF (1:500, Millipore, AB7356), CA9 (1:100, Genetex, GTX70020), H3K27Me3 (1:1000, Millipore, 07-689), H2AK119Ub (1:500, Cell signaling, #8240S), CD15 (1:100, Millipore, MAB4301), Ki67 (1:100, Dako, M7240), active CASPASE3 (1:100, Cell signaling, #9661S) and the secondary fluorescence-labeled antibodies. Nuclei were counterstained with DAPI. Immunofluorescence images were taken by a LEICA TCS SP5 Confocal Microscope or a Leica SCN400 Slide Scanner. A Senescence β-Galctosidase Staining Kit (Cell Signaling, 9860S) was used to detect senescent cells in tumor tissues, the phase-contrast light images were captured by Leica DM4000 B microscope.

Tissue microarray (TMA) and Immunohistochemistry

5 μm thick slides of de-identified paraffin-embedded tissue microarrays (TMAs) were constructed from glioma after obtaining Ohio State University Institutional Review Board Approval. A total of 96 cases were arrayed on the TMA block, including 15 non-neoplastic controls (cortical dysplasias), 16 grade II glioma cases, 27 grade III gliomas, and 38 grade IV glioblastomas. Tissues too small and/or crushed on the TMA were eliminated from analysis after immunohistochemistry staining with anti-BMI1 (1:50, Abcam, ab126783), anti-EZH2 (1:100, BD Biosciences, 612667), anti-CD44 (1:100, BD Biosciences, 550392), anti-OLIG2 (1:100, R&D system, AF2418), and secondary HRP-conjugated antibodies. The TMA images were taken by a Leica SCN400 Slide Scanner. Overall staining on TMA was scored as – (negative) or + (positive) compared to non-neoplastic controls. PN3691 (with or without treatment with BMI1 or EZH2 inhibitors) xenografted brain tissues were fixed in 4% paraformaldehyde, and were stained with anti-H2K119Ub (1:100, Cell signaling, #8240S), anti-H3K27Me3 (1:1000, Millipore, 07-689), and secondary HRP-conjugated antibodies. Nuclei in immunohistochemistry were counterstained with Hematoxylin. The immunohistochemistry images were taken by a LEICA DM4000B Microscope, and were analyzed by IHC Profiler.

Cell viability and cell growth assays

Cell viability was measured by CellTiter-Glo Luminescent Cell Viability Assay (Promega) according to manufacturer's instructions after exposing 3 days under different conditions including low-glucose (0.45 g/l glucose)[10], hypoxia (1% oxygen)[7], BMI1 inhibitor (PTC596, PTC therapeutics; PTC209, PTC therapeutics), and EZH2 inhibitor (EPZ6438, Medchemexpress LLC; DZNep, SELLECKCHEM). 1×10^6 cells were seeded for cell viability under low-glucose or/and hypoxia conditions, 2×10^3 cells were seeded for drug response under BMI1 or EZH2 inhibitor treatment. IC50 values of BMI1 or EZH2 inhibitors were calculated with GraphPad Prism software. For competitive response assay of BMI1 and EZH2 inhibitors, the proportion of GFP or mCherry positive cells was determined by flow cytometry after treatment the co-cultured MES83-GFP and PN528-mCherry cells with PTC-209, and DZNep. Two-dimensional titration assay was performed on four different subtype GSCs after combined treatment with different doses of PTC596 and EPZ6438. Relative cell growth was measured over a four-day time course using CellTiter-Glo Luminescent Cell Viability Assay kit (Promega) after seeding 1×10^3 cells.

In vitro limiting dilution tumorsphere formation assay

For detection of stem cell frequency change by BMI1 and EZH2 signaling pathway, different numbers of cells per well (range of 40 to 1 cell/well) were seeded in 96-well plates containing 100 μl completed neurobasal medium with or without BMI1 or/and EZH2 inhibitors, and added 20 μl completed neurobasal medium with or without BMI1 or/and EZH2 inhibitors per 3 days. After 14 days, the tumorspheres were measured, and were analyzed by Extreme Limiting Dilution analysis software (http://bioinf.wehi.edu.au/software/elda).

Plasmid and lentiviral or retroviral transduction

Lentiviral plasmids for targeting EZH2 (TRCN0000040077 for shEZH2-950, and TRCN0000293738 for shEZH2-2450), BMI1 (TRCN0000020158 for swhBMI1-880, and TRCN0000020157 for shBMI1-939), RNF144A (TRCN0000004414 for shRNF144A-1099, and TRCN0000004416 for shRNF144A-3112) and non-specific control sequence (SCH002 for shCNTRL) were purchased from Sigma-Aldrich. Lentiviral plasmids pGIPZ-GFP, PRSC-mCherry, L-2-G, and L-2-T were used to label the BTIC cells in *in vivo* experiments. Lentiviral particles were produced in 293T cells with PAX2 and PMD2G helper plasmids (Addgene) in stem cell medium. Retroviral plasmids PMSC-BMI1 and PMSC-VEC (control) were used to produce retroviral particles in 293T cells with pCMV-VSVG and pCMV-Gag-Pol helper plasmids (Addgene).

Calculation of achievable drug concentrations

Zhang and co-workers reported the pharmacokinetics of the EZH2 inhibitor, EPZ6438, in combination with the ABCB1 and ABCG2 inhibitor, Elacridar[40]. They found that the EPZ6438 concentration was 1.5 μg/ml in the plasma and 0.35 mg/kg in the brain 1 hour after treatment with 2.5 mg/kg EPZ6438 and 100 mg/kg Elacridar. Based on these observations and the likely contamination of the brain measurements by blood, we calculated the minimum brain concentration as $(1.5 \times 0.35)/2.5 = 0.21$ μg/ml. Our studies used 350 mg/kg of EPZ6438 (e.g. 140-fold higher dose), leading to a calculated brain concentration of 29 – 210 μg/ml. The molecular weight of EPZ6438 is 572.74, translating into a calculated brain concentration range of 51 – 366 μM. We determined the concentration of the BMI1 inhibitor 4 hours after combined treatment with 10 mg/kg or 12.5 mg/kg BMI1 inhibitor PTC596 (MW 420.34) and 350 mg/kg EZH2 inhibitor EPZ6438 in the plasma and brain. 10 mg/kg BMI1 inhibitor treatment achieved 1 μg/ml in plasma and 2 mg/kg in the brain. Using the same approach that we used for the EZH2 inhibitor concentration calculations, we estimated the brain concentration range of the BMI1 inhibitor administered at 10 mg/kg as 475.8 – 2379 nM. Collectively, in vivo drug ranges for each agent achieved concentrations consistent with those we detected as having combinational benefit in IC80 concentrations from two-dimensional drug concentration assays [51.3 – 366.7 μM for the EZH2 inhibitor and 158.6 – 793 nM (1/3 of 475.8 – 2379 nM) for the BMI1 inhibitor].

Animal experiments

All animal studies were performed in accordance with Cleveland Clinic IACUC approved protocols. Required sample sizes were calculated by an a priori power analysis. All mice

were randomly assigned to appropriate treatment groups. For the co-implantation study, 2.5 × 10^5 PN3691-mCherry-BMI1 and 2.5 × 10^5 PN3691-GFP-VEC cells (BMI1/VEC), or 5 × 10^5 PN3691-GFP-VEC (VEC/VEC control) cells were implanted into the right frontal lobes of 3 weeks old NOD SCID gamma (NSG) mice as previously described[7]. For pharmacokinetic study, BMI1 inhibitor (PTC596) concentration in plasma and brain was determined by HPLC-mass after oral administration of BMI1 inhibitor (PTC596) or EZH2 inhibitor (EPZ6438) with Elacridar (dual ABCCB1 and ABCG2 inhibitor; Medchemexpress LCC) to enhance EPZ6438 uptake into brain[39]. For pharmacodynamic testing of BMI1 and EZH2 inhibitors, 5 × 10^5 PN3691 cells were implanted intracranially into NSG mice. After 1 week, the BMI1 inhibitor (PTC596) or EZH2 inhibitor (EPZ6438) with Elacridar were administered orally by gavage. For testing, *in vivo* inhibition effect of BMI1 and EZH2 inhibitors, 1 × 10^5 luciferase-expressing PN1919 or MES20 cells for single subtype glioblastoma model, and 1000 RFP-labeled PN1919 and 1000 GFP-labeled MES20 cells for subtype-mixed glioblastoma model were implanted intracranially into NSG mice. When the luciferase signals from tumor cells were detectable (after 4 days for single subtype model, and 10 days for subtype-mixed model), the BMI1 inhibitor or EZH2 inhibitor with Elacridar were administered orally by gavage. The size of orthotopic tumor was monitored by bioluminescence channel of IVIS Spectrum. The investigators were blinded to the group allocation and study outcome assessments of all mice.

Chromatin immunoprecipitation (ChIP) assay

Chromatin immunoprecipitation (ChIP) of 5–10 mg of flash frozen primary glioblastoma tumors, and 1 million fresh CD15+ GSCs was performed using H3K27Ac (5 mg; Active Motif, 39133), H3K27Me3 (5 mg; Active Motif, 39155), and H2AK119Ub (10 mg, Cell signaling, #8240S) antibodies per ChIP experiment (Abcam, AB4729). Enriched DNA was quantified using Picogreen (Invitrogen) and ChIP libraries were amplified and barcoded using the Thruplex DNA-seq library preparation kit (Rubicon Genomics) according to manufacturer recommendations. Following library amplification, DNA fragments were Agarose gel (1.0%) size selected (< 1 kb), assessed using Bioanalyzer (Agilent Technologies) and sequenced at The Center for Applied Genomics (The Hospital for Sick Children) using Illumina Hi-Seq2000 100 bp single-end sequencing. Sequencing reads were aligned using Bowtie2 to the hg19 genome using default settings. HOMER was used for calling peaks in the H3K27me3 and H2AK119ub datasets versus ChIP Input data with the following settings: -F 2, -P 0.01, -L 2, -LP 0.01, -minDist 5000 –size 1000. Region specific peaks were identified using the BedTools subtract function and overlapping peaks were defined using the BedTools intersect function. Gene Ontology Pathway analysis was performed using the gene set enrichment analysis molecular signatures database at (http://software.broadinstitute.org/gsea/index.jsp) and using the HOMER annotatePeaks function. Molecular Signature bubble plots were created using Cytoscape v3.5 and the Bader Lab Enrichment Map software (http://www.baderlab.org/Software/EnrichmentMap). All raw ChIP sequencing data may be accessed from the NCBI Gene Expression Omnibus (GEO GSE86237).

RNA sequencing

Total RNA was extracted with TRIzol (Invitrogen), separated using Phase Lock Gel tubes (5 Prime), and purified using the miRNAeasy kit (Qiagen). Total RNA was prepared for sequencing by Beckman-Coulter Genomics using the Illumina TruSeq Stranded Total RNA Library Prep Kit. RNA-seq libraries were sequenced on the Illumina HiSeq 2500 platform by Beckman-Coulter Genomics. For gene expression analysis, reads were aligned to the hg19 genome build (retrieved from http://cufflinks.cbcb.umd.edu/igenomes.html), using Tophat v2.0.6. Paired-end 125-bp reads were generated on an Illumina HiSeq 2500 instrument at the Case Western Reserve University Genomics Core Facility. Reads were aligned to the hg19 genome using TopHat v2.0.6 with the library type option set to first strand. FPKM values for known genes were calculated using Cufflinks v2.0.2 provided with the GTF file via the -G (known genes only) option. FPKM values were Quantile Normalized. All RNA sequencing raw data may be accessed from the NCBI Gene Expression Omnibus (GEO GSE86237).

In silico analyses

Collected in silico resources, including transcript microarray data, RNA sequencing, patient survival, and anatomic information of patient samples were downloaded from TCGA (https://tcga-data.nci.nih.gov/tcga) and Ivy GAP (http://glioblastoma.alleninstitute.org) portal websites. GBM molecular subtypes (including proneural, classical, and mesenchymal), EZH2 and BMI1 activation or inhibition signatures were informed by previous publications[36, 37, 65]. Microenvironment-related gene signatures included: mature-vascular signature (MATURE_VAS), 9 genes significantly up-regulated twofold in HUVEC compared to HMEC (Supplementary Fig. 2a and 2b); microvascular signature (MICRO_VAS), 8 genes significantly up-regulated twofold in HMEC compared to HUVEC (Supplementary Fig. 2a and 2b); hypoxia activation signature (HYPOXIA_AC), 9 genes significantly up-regulated twofold in hypoxia regions compared to normoxia region (Supplementary Fig. 3a and 3b); hypoxia inhibition signature (HYPOXIA_IN), 23 genes significantly down-regulated in hypoxia regions compared to normoxia regions (Supplementary Fig. 3a and 3b). Single sample GSEA (ssGSEA) was used to analyze gene signature enrichment in TCGA and Ivy GAP datasets. Correlation of genes and signatures was analyzed by Excel software, and the patient survival was analyzed with GraphPad Prism software.

Statistical analysis

All grouped data are presented as mean ± standard error of the mean (SEM). Significance between groups was analyzed by one-way ANOVA or Student's t-test using GraphPad Prism software. The F-values and DF for each ANOVA test can be found in the Life Sciences Reporting Summary associated with this manuscript. Correlation coefficients were calculated by Excel software. Kaplan-Meier survival curves were generated by GraphPad Prism software, and log-rank p-value were used to determine significance. All experiments were repeated in each specimen presented in at least three biologic duplicates (patient-derived xenograft cell models) with technical triplicates. Multivariate linear regression was performed using R 3.2.4. Independent variables were tumor type by histology (astrocytoma,

oligoastrocytoma, oligodendroglioma, or glioblastoma), IDH1 mutation status (wild-type vs. mutant), chromosome 1p/19q co-deletion (co-deleted vs. non-co-deleted) and ATRX status (wild-type vs. mutant). Sample size was determined using the appropriate power calculation formula in JMP (Version 12, SAS Institute Inc., Cary, NC, 1989–2007) for each experimental setup. This study complies with randomization. The investigator was blinded to the group allocation during the experiment and/or when assessing the outcome.

Supplementary Material

Refer to Web version on PubMed Central for supplementary material.

Acknowledgments

References

1. Wen PY, Kesari S. Malignant Gliomas in Adults. N Engl J Med. 2008; 359:492–507. [PubMed: 18669428]

2. Singh SK, et al. Identification of human brain tumour initiating cells. Nature. 2004; 432:396–401. [PubMed: 15549107]

3. Galli R, et al. Isolation and Characterization of Tumorigenic, Stem-like Neural Precursors from Human Glioblastoma. Cancer Res. 2004; 64:7011–7021. [PubMed: 15466194]

4. Jin X, et al. Blockade of EGFR signaling promotes glioma stem-like cell invasiveness by abolishing ID3-mediated inhibition of p27KIP1 and MMP3 expression. Cancer Lett. 2013; 328:235–242. [PubMed: 23022473]

5. Bao S, et al. Glioma stem cells promote radioresistance by preferential activation of the DNA damage response. Nature. 2006; 444:756–760. [PubMed: 17051156]

6. Bao S, et al. Stem Cell–like Glioma Cells Promote Tumor Angiogenesis through Vascular Endothelial Growth Factor. Cancer Res. 2006; 66:7843–7848. [PubMed: 16912155]

7. Li Z, et al. Hypoxia-Inducible Factors Regulate Tumorigenic Capacity of Glioma Stem Cells. Cancer Cell. 2009; 15:501–513. [PubMed: 19477429]

8. Calabrese C, et al. A Perivascular Niche for Brain Tumor Stem Cells. Cancer Cell. 2007; 11:69–82. [PubMed: 17222791]

9. Hjelmeland AB, et al. Acidic stress promotes a glioma stem cell phenotype. Cell Death Differ. 2011; 18:829–840. [PubMed: 21127501]

10. Flavahan WA, et al. Brain tumor initiating cells adapt to restricted nutrition through preferential glucose uptake. Nat Neurosci. 2013; 16:1373–1382. [PubMed: 23995067]

11. Verhaak RGW, et al. Integrated Genomic Analysis Identifies Clinically Relevant Subtypes of Glioblastoma Characterized by Abnormalities in PDGFRA, IDH1, EGFR, and NF1. Cancer Cell. 2010; 17:98–110. [PubMed: 20129251]

12. Oh YT, et al. Translational Validation of Personalized Treatment Strategy Based on Genetic Characteristics of Glioblastoma. PLOS ONE. 2014; 9:e103327. [PubMed: 25084005]

13. Patel AP, et al. Single-cell RNA-seq highlights intratumoral heterogeneity in primary glioblastoma. Science. 2014; 344:1396–1401. [PubMed: 24925914]

14. Meyer M, et al. Single cell-derived clonal analysis of human glioblastoma links functional and genomic heterogeneity. Proc Natl Acad Sci. 2015; 112:851–856. [PubMed: 25561528]

15. Halliday J, et al. In vivo radiation response of proneural glioma characterized by protective p53 transcriptional program and proneural-mesenchymal shift. Proc Natl Acad Sci. 2014; 111:5248–5253. [PubMed: 24706837]

16. Bhat KPL, et al. Mesenchymal Differentiation Mediated by NF-κB Promotes Radiation Resistance in Glioblastoma. Cancer Cell. 2013; 24:331–346. [PubMed: 23993863]

17. Mao P, et al. Mesenchymal glioma stem cells are maintained by activated glycolytic metabolism involving aldehyde dehydrogenase 1A3. Proc Natl Acad Sci. 2013; 110:8644–8649. [PubMed: 23650391]

18. Joo KM, et al. Patient-Specific Orthotopic Glioblastoma Xenograft Models Recapitulate the Histopathology and Biology of Human Glioblastomas In Situ. Cell Rep. 2013; 3:260–273. [PubMed: 23333277]

19. Hägerstrand D, et al. Identification of a SOX2-dependent subset of tumor- and sphere-forming glioblastoma cells with a distinct tyrosine kinase inhibitor sensitivity profile. Neuro-Oncol. 2011; 13:1178–1191. [PubMed: 21940738]

20. Park TS, et al. Vascular Progenitors from Cord Blood-Derived iPSC Possess Augmented Capacity for Regenerating Ischemic Retinal Vasculature. Circulation. 2013; CIRCULATIONAHA. 113.003000. doi: 10.1161/CIRCULATIONAHA.113.003000

21. Marotta D, et al. In Vivo Profiling of Hypoxic Gene Expression in Gliomas Using the Hypoxia Marker EF5 and Laser-capture Microdissection. Cancer Res. 2011; 71:779–789. [PubMed: 21266355]

22. Gynther M, et al. Large Neutral Amino Acid Transporter Enables Brain Drug Delivery via Prodrugs. J Med Chem. 2008; 51:932–936. [PubMed: 18217702]

23. Masouyé I, et al. Endothelial Cells of the Human Microvasculature Express Epidermal Fatty Acid–Binding Protein. Circ Res. 1997; 81:297–303. [PubMed: 9285630]

24. Graeber TG, et al. Hypoxia-mediated selection of cells with diminished apoptotic potential in solid tumours. Nature. 1996; 379:88–91. [PubMed: 8538748]

25. Begg AC, Stewart FA, Vens C. Strategies to improve radiotherapy with targeted drugs. Nat Rev Cancer. 2011; 11:239–253. [PubMed: 21430696]

26. Tavares L, et al. RYBP-PRC1 Complexes Mediate H2A Ubiquitylation at Polycomb Target Sites Independently of PRC2 and H3K27me3. Cell. 2012; 148:664–678. [PubMed: 22325148]

27. Son MJ, Woolard K, Nam DH, Lee J, Fine HA. SSEA-1 Is an Enrichment Marker for Tumor-Initiating Cells in Human Glioblastoma. Cell Stem Cell. 2009; 4:440–452. [PubMed: 19427293]

28. Wang H, et al. Role of histone H2A ubiquitination in Polycomb silencing. Nature. 2004; 431:873–878. [PubMed: 15386022]

29. Kamminga LM, et al. The Polycomb group gene Ezh2 prevents hematopoietic stem cell exhaustion. Blood. 2006; 107:2170–2179. [PubMed: 16293602]

30. Douglas D, et al. BMI-1 Promotes Ewing Sarcoma Tumorigenicity Independent of CDKN2A Repression. Cancer Res. 2008; 68:6507–6515. [PubMed: 18701473]

31. Lu C, et al. Regulation of Tumor Angiogenesis by EZH2. Cancer Cell. 2010; 18:185–197. [PubMed: 20708159]

32. Ho SR, Mahanic CS, Lee YJ, Lin WC. RNF144A, an E3 ubiquitin ligase for DNA-PKcs, promotes apoptosis during DNA damage. Proc Natl Acad Sci. 2014; 111:E2646–E2655. [PubMed: 24979766]

33. Zhang P, et al. ABCB1 and ABCG2 restrict the brain penetration of a panel of novel EZH2-Inhibitors. Int J Cancer. 2015; 137:2007–2018. [PubMed: 25868794]

34. Venteicher AS, et al. Decoupling genetics, lineages, and microenvironment in IDH-mutant gliomas by single-cell RNA-seq. Science. 2017; 355:eaai8478. [PubMed: 28360267]

35. Piccirillo SGM, et al. Distinct pools of cancer stem-like cells coexist within human glioblastomas and display different tumorigenicity and independent genomic evolution. Oncogene. 2009; 28:1807–1811. [PubMed: 19287454]

36. Segerman A, et al. Clonal Variation in Drug and Radiation Response among Glioma-Initiating Cells Is Linked to Proneural-Mesenchymal Transition. Cell Rep. 2016; 17:2994–3009. [PubMed: 27974212]

37. Jung J, et al. Nicotinamide metabolism regulates glioblastoma stem cell maintenance. JCI Insight. 2017; 2

38. Gilbertson RJ, Rich JN. Making a tumour's bed: glioblastoma stem cells and the vascular niche. Nat Rev Cancer. 2007; 7:733–736. [PubMed: 17882276]

39. Brennan CW, et al. The Somatic Genomic Landscape of Glioblastoma. Cell. 2013; 155:462–477. [PubMed: 24120142]

40. Turcan S, et al. IDH1 mutation is sufficient to establish the glioma hypermethylator phenotype. Nature. 2012; 483:479–483. [PubMed: 22343889]

41. Rohle D, et al. An Inhibitor of Mutant IDH1 Delays Growth and Promotes Differentiation of Glioma Cells. Science. 2013; 340:626–630. [PubMed: 23558169]

42. Chan KM, et al. The histone H3.3K27M mutation in pediatric glioma reprograms H3K27 methylation and gene expression. Genes Dev. 2013; 27:985–990. [PubMed: 23603901]

43. Project S. J. C. R. H.-W. U. P. C. G. Somatic histone H3 alterations in pediatric diffuse intrinsic pontine gliomas and non-brainstem glioblastomas. Nat Genet. 2012; 44:251–253. [PubMed: 22286216]

44. Schwartzentruber J, et al. Driver mutations in histone H3.3 and chromatin remodelling genes in paediatric glioblastoma. Nature. 2012; 482:226–231. [PubMed: 22286061]

45. Mazor T, et al. DNA Methylation and Somatic Mutations Converge on the Cell Cycle and Define Similar Evolutionary Histories in Brain Tumors. Cancer Cell. 2015; 28:307–317. [PubMed: 26373278]

46. Bruggeman SWM, et al. Bmi1 Controls Tumor Development in an Ink4a/Arf-Independent Manner in a Mouse Model for Glioma. Cancer Cell. 2007; 12:328–341. [PubMed: 17936558]

47. Abdouh M, et al. BMI1 Sustains Human Glioblastoma Multiforme Stem Cell Renewal. J Neurosci. 2009; 29:8884–8896. [PubMed: 19605626]

48. Godlewski J, et al. Targeting of the Bmi-1 Oncogene/Stem Cell Renewal Factor by MicroRNA-128 Inhibits Glioma Proliferation and Self-Renewal. Cancer Res. 2008; 68:9125–9130. [PubMed: 19010882]

49. Venugopal C, et al. Bmi1 marks intermediate precursors during differentiation of human brain tumor initiating cells. Stem Cell Res. 2012; 8:141–153. [PubMed: 22265735]

50. Gargiulo G, et al. In Vivo RNAi Screen for BMI1 Targets Identifies TGF-β/BMP-ER Stress Pathways as Key Regulators of Neural- and Malignant Glioma-Stem Cell Homeostasis. Cancer Cell. 2013; 23:660–676. [PubMed: 23680149]

51. Kreso A, et al. Self-renewal as a therapeutic target in human colorectal cancer. Nat Med. 2014; 20:29–36. [PubMed: 24292392]

52. Lee J, et al. Epigenetic-Mediated Dysfunction of the Bone Morphogenetic Protein Pathway Inhibits Differentiation of Glioblastoma-Initiating Cells. Cancer Cell. 2008; 13:69–80. [PubMed: 18167341]

53. Suvà ML, et al. EZH2 Is Essential for Glioblastoma Cancer Stem Cell Maintenance. Cancer Res. 2009; 69:9211–9218. [PubMed: 19934320]

54. Kim E, et al. Phosphorylation of EZH2 Activates STAT3 Signaling via STAT3 Methylation and Promotes Tumorigenicity of Glioblastoma Stem-like Cells. Cancer Cell. 2013; 23:839–852. [PubMed: 23684459]

55. Fan TY, et al. Inhibition of EZH2 reverses chemotherapeutic drug TMZ chemosensitivity in glioblastoma. Int J Clin Exp Pathol. 2014; 7:6662–6670. [PubMed: 25400745]

56. Mohammad F, et al. EZH2 is a potential therapeutic target for H3K27M-mutant pediatric gliomas. Nat Med. 2017; 23:483–492. [PubMed: 28263309]

57. Piunti A, et al. Therapeutic targeting of polycomb and BET bromodomain proteins in diffuse intrinsic pontine gliomas. Nat Med. 2017; 23:493–500. [PubMed: 28263307]

58. Facchino S, Abdouh M, Chatoo W, Bernier G. BMI1 Confers Radioresistance to Normal and Cancerous Neural Stem Cells through Recruitment of the DNA Damage Response Machinery. J Neurosci. 2010; 30:10096–10111. [PubMed: 20668194]

59. Wu Z, et al. Combined aberrant expression of Bmi1 and EZH2 is predictive of poor prognosis in glioma patients. J Neurol Sci. 2013; 335:191–196. [PubMed: 24139839]

60. Wang Q, et al. Tumor evolution of glioma intrinsic gene expression subtype associates with immunological changes in the microenvironment. bioRxiv. 2016; 52076doi: 10.1101/052076
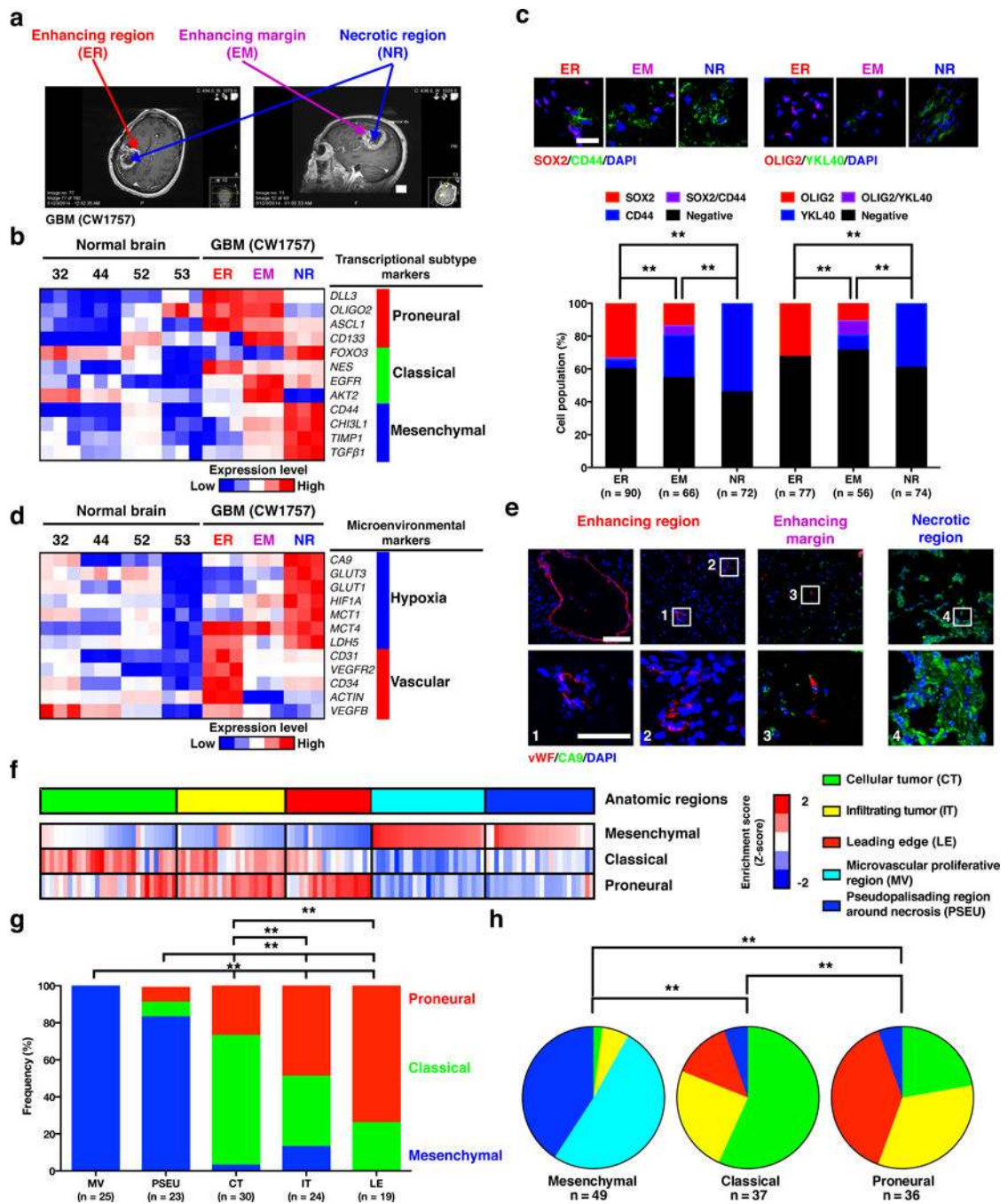
Figure 1. Anatomical distribution of transcriptional profiles in glioblastoma

(**a**) T1-weighted MRI images of multiregional glioblastoma sampling process (representative of four patients) for qPCR and immunofluorescence analysis. (**b**) A heatmap of molecular subtype maker expression in three multiregional glioblastoma samples and four non-malignant human brain samples. Z-scores were calculated from qPCR ΔC_t values. (**c**) Immunofluorescence images (representative of 10 fields for each region) showing SOX2 (red), CD44 (green), OLIG2 (red), and YKL40 (green) positive cells in multiregional glioblastoma samples. Scale bar, 25 μm. SOX2, CD44, OLIG2, and YKL40 positive cells

were compared by Chi-square test. **, p < 0.001. (**d**) Heatmap showing the expression of markers of hypoxia (*CA9*, *GLUT3*, *GLUT1*, *HIF1α*, *MCT1*, *MCT4*, and *LDH5*) and vascular (*CD31*, *VEGFR2*, *CD34*, *ACTIN*, and *VEGFB*) in three multiregional glioblastoma samples and four non-malignant human brain samples. Z-scores were calculated from qPCR ΔC_t values. (**e**) Immunofluorescence images (representative from three fields for each region) showing vWF (red) and CA9 (green) positive locations in multiregional glioblastoma samples. Scale bar upper panels, 25 μm. Scale bar lower panels, 10 μm. (**f**) Heatmap showing Z-scores of each glioblastoma subtype signature normalized within each patient sample set determined via ssGSEA for each RNA-sample in the Anatomic Structure Study dataset (RNA-sample $n = 122$; patient $n = 10$) from the Ivy Glioblastoma Atlas Project (Ivy GAP) database. The corresponding histological feature for each RNA-sample is labeled above: Pseudopallisading cells around necrosis (PSEU); microvascular proliferative region (MV); cellular tumor (CT); leading edge (LE); infiltrating tumor (IT). (**g, h**) Chi-square test of glioblastoma histological feature distributions among transcriptional profiles and molecular subtype distribution among histological structures, respectively. **, p < 0.001.
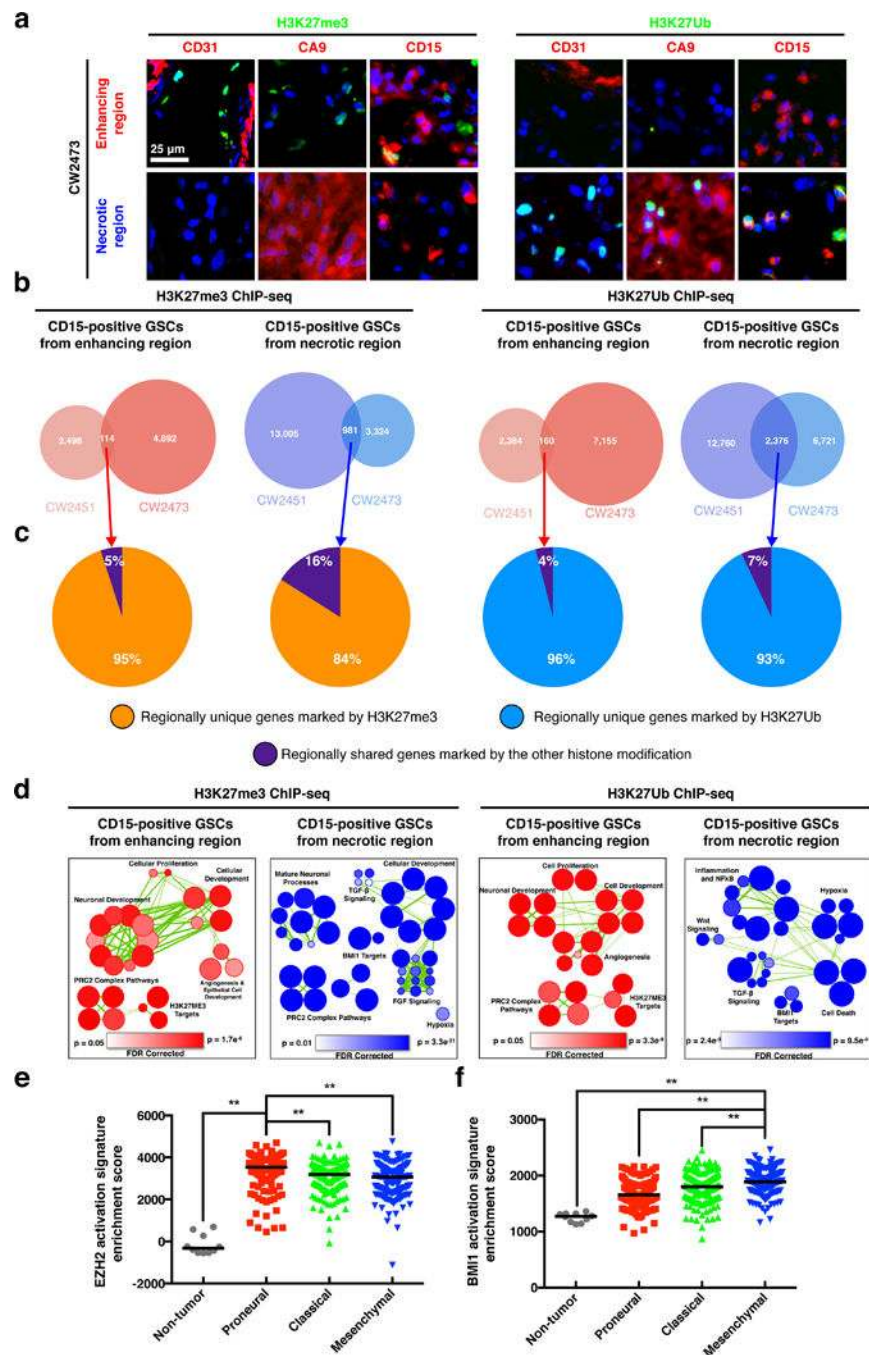
Figure 2. Epigenetic GSC signatures in multi-regional primary specimens

(**a**) Immunofluorescence images showing CD31 (red), CA9 (red), CD15 (red), H3K27Me3 (green), and H2AK119Ub (green) positive location and cells in multiregional glioblastoma samples. Scale bar, 25 μm. (**b**) Overlap in regional specific H3K27me3 or H2AK119Ub binding genes in CW2451- and CW2473-derived CD15 positive glioma cells. Venn diagrams showing overlaps between region specific peaks derived from H3K27me3 or H2AK119Ub ChIP-seq experiments on two primary glioblastoma specimens. (**c**) Pie graph showing fraction of regional unique target genes by H3K27Me3 or H2AK119Ub from the

overlapping region specific genes shown in (**b**). (**d**) Gene ontology bubble plots showing gene signatures enriched in the overlapping region specific peaks shown in (**b**). (**e, f**) Enrichment levels of EZH2 (**e**) or BMI1 (**f**) activation signatures in transcriptional subgroups from the TCGA glioblastoma dataset (n = 10, Non-tumor; n = 161, Proneural; n = 209, Classical; n = 167, Mesenchymal). Data shows the median value (black bars). **, $p < 0.01$; by one-way ANOVA with Tukey's method for multiple comparisons.
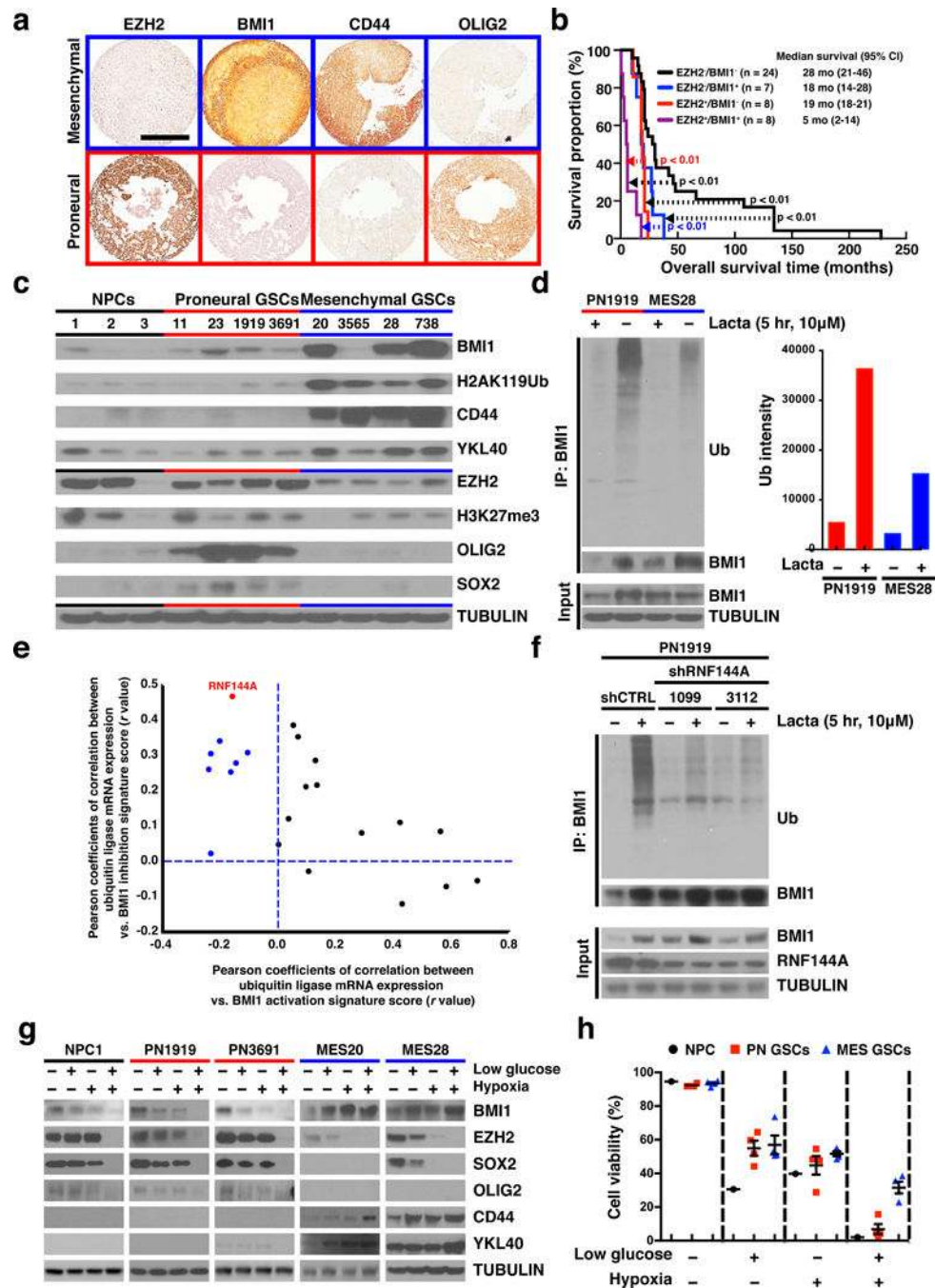
Figure 3. Differential polycomb repressive complex function in glioblastoma subgroups
(**a**) Representative images of glioblastoma tissue microarray samples (n = 96) showing the expression of EZH2, BMI1, CD44, and OLIG2. Scale bar, 500 μm. (**b**) Kaplan-Meier curve of patient survival stratified by EZH2 and BMI1 protein expression level from a glioblastoma tissue microarray. Log-rank p-values were used to determine statistics significance. (**c**) Cell lysates were prepared from neural progenitor cells (NPC1, NPC2, and NPC3), proneural GSCs 670 (PN11, PN23, PN1919, and PN3691), and mesenchymal GSCs (MES20, MES3565, MES28, MES738). Protein was resolved by SDS-PAGE. Immunoblot

for performed for BMI1, H2K119Ub, EZH2, H3K27me3, and markers for mesenchymal (CD44 and YKL40) and proneural (OLIG2 and SOX2) glioblastoma. (**d**) Immunoprecipitation followed by immunoblot was performed for BMI1 polyubiquitination in PN1919 and MES28 cells in presence or absence of lactacystin treatment for 5 hours (Lacta, 10 μM). Right panel: quantification of BMI1 polyubiquitination by Image J. Data normalized by input loading controls. (**e**) Rank-ordered list of correlation coefficients (*r* values) between ubiquitin ligases and BMI1 activation or inhibition signatures in TCGA glioblastoma samples. (**f**) BMI1 polyubiquitination by RNF144A in PN1919 cells after transduction with shRNA control (shCTRL) or shRNF144A (shRNF144A-1099 and shRNF144A-3112) was examined by immunoprecipitation of BMI1 followed by immunoblotting for BMI1 or ubiquitin in presence or absence of lactacystin treatment for 5 hours (Lacta, 10 μM). Levels of BMI1, RNF144A, and TUBULIN were measured by immunoblot in the input whole cell lysates. (**g**) Neural progenitor cells (NPC1), proneural GSCs (PN1919 and PN3691), and mesenchymal GSCs (MES20 and MES28) were grown under baseline, low-glucose, hypoxia, or combined conditions. Levels of RNF144A, BMI1, EZH2, CD44, YKL40, OLIG2, and SOX2 proteins were measured by immunoblot. (**h**) Cell viability of neural progenitor cells (NPC1), proneural GSCs (PN11, PN23, PN1919, and PN3691), and mesenchymal GSCs (MES20, MES28, MES3565, and MES738) were determined under baseline, low-glucose, hypoxia, or combined conditions. Data are presented as mean ± SEM. *, $p < 0.05$; by Wilcoxon and Mann-Whitney t-test.
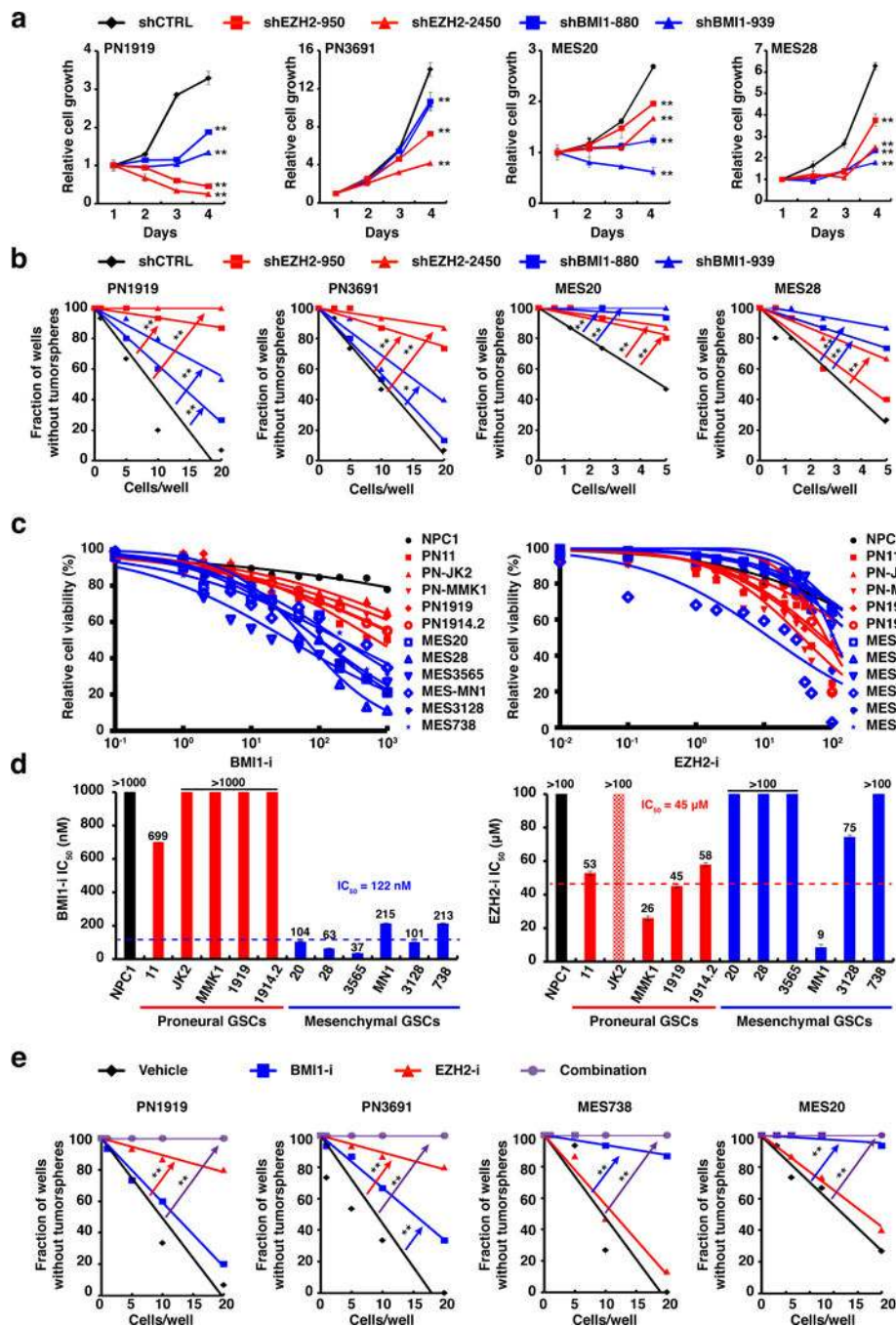
Figure 4. Differential efficacy of BMI1 and EZH2 inhibitors against glioblastoma subgroups
(**a**) Cell growth rates of GSCs transduced with shRNA control (shCNTRL), EZH2-knockdown (shEZH2-950 and shEZH2-2450) or BMI1-knockdown (shBMI1-880 and shBMI1-939) (n = 5 per group and time point). Data shows mean ± SEM. **, p < 0.01; by one-way ANOVA with Dunnett's multiple-comparison test. (**b**) *In vitro* limited dilution assay of GSCs transduced with shRNA control (shCNTRL), EZH2-knockdown (shEZH2-950 and shEZH2-2450) or BMI1-knockdown (shBMI1-880 and shBMI1-939) (n = 15 per group). **, p < 0.01; by Chi-square test. (**c**) Cell viability curves of neural progenitors

(NPC1), proneural GSCs (PN11, PN-JK2, PN-MMK1, PN1919, and PN1914.2), or mesenchymal GSCs (MES20, MES28, MES3565, MES-MN1, MES3128, and MES738) after treatment with increasing concentrations of (left) BMI1 inhibitor (BMI1-i, PTC596) or (right) EZH2 inhibitor (EZH2-i, EPZ6438). (**d**) IC$_{50}$ of BMI1-i (left graph) or EZH2-i (right graph) for indicated cells. (**e**) *In vitro* limited dilution assay of PN1919, PN3691, MES738, and MES20 cells after treatment with vehicle control, 10 nM BMI1-i, 5 μM EZH2-i, or the combined treatment ($n = 15$ per group). **, p < 0.01; by Chi-square test.
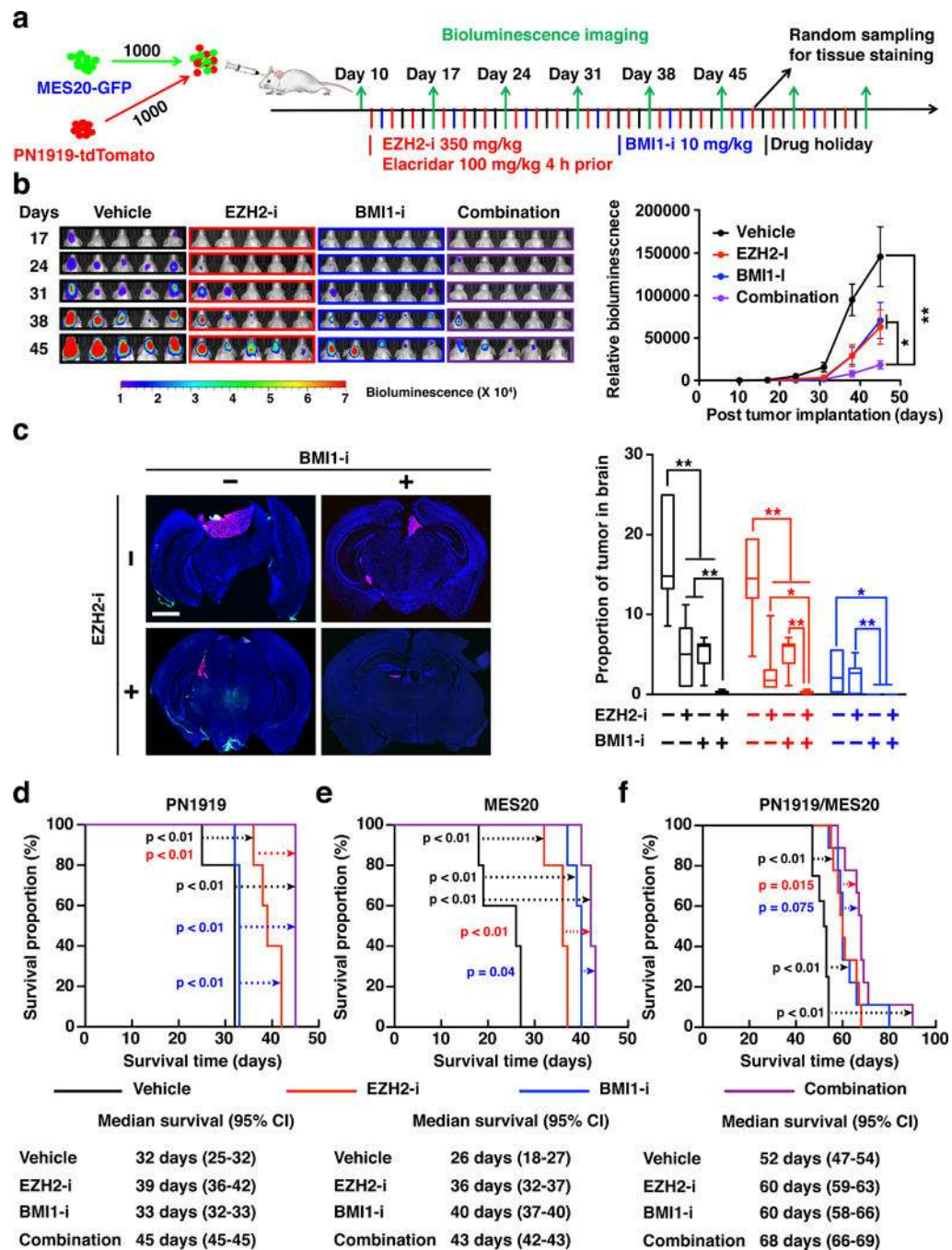
Figure 5. *In vivo* therapeutic efficacy of combined pharmacologic inhibition of BMI1 and EZH2 on subtype-mixed glioblastoma model

(**a**) Experimental design for in vivo effects of BMI1 (PTC596) and EZH2 (EPZ6438) inhibitors on xenograft of mixed proneural and mesenchymal GSCs. (**b**) Bioluminescence images of mice bearing mixed proneural and mesenchymal xenografts derived from luciferase-expressing PN1919 and MES20 cells, showing the effect of combined treatment of 10 mg/kg BMI1-i per week and 350 mg/kg EZH2-i thrice weekly on tumor growth. Right panels: Quantification of bioluminescence signals during 45 days of treatment in mice

implanted with luciferase-expressing PN1919 and MES20 cells. The signals were normalized to day 10 signaling intensity for each mouse ($n = 10$ per group and time point). *, $p < 0.05$; **, $p < 0.01$; by one-way ANOVA with Tukey's method for multiple comparisons. (**c**) Whole brain images showing distribution of PN1919 (red) and MES20 (green) population in the intermediate tumor samples (day 48). Right panel: Quantification of relative area of occupied by PN1919 (red), MES20 (green), and total tumor population in the intermediate tumor samples. Vehicle control, $n = 10$; EZH2-i alone, $n = 15$; BMI1-i alone, $n = 14$; combined treatment, $n = 10$. *, $p < 0.01$; **, $p < 0.01$; by one-way ANOVA with Tukey's method for multiple comparisons. (**d, e**) Kaplan-Meier survival curve of orthotopic tumor-bearing mice with PN1919 (**d**) or MES20 (**e**) cells under the combined treatment of 12.5 mg/kg BMI1-i and 350 mg/kg 710 EZH2-i ($n = 5$ per group). Log-rank p-values were used to determine statistics significance. (**f**) Kaplan-Meier survival curve of subtype-mixed orthotopic tumor-bearing mice with PN1919 and MES20 cells upon the combined treatment of 10 mg/kg BMI1-i per week and 350 mg/kg EZH2-i thrice weekly ($n = 8$ per group). Log-rank p-values were used to determine statistics significance.